Robotica (2010) volume 28, pp. 675–687. © Cambridge University Press 2009
doi:10.1017/S0263574709990324

A shape memory alloy based tendon-driven actuation system for biomimetic artificial fingers, part II: modelling and control

Gabriele Gilardi†, Edmund Haslam†, Vishalini Bundhoo† and Edward J. Park†,‡,*

†*Department of Mechanical Engineering, University of Victoria, PO Box 3055 STN CSC, Victoria, BC, Canada V8W 3P6*
‡*Mechatronic Systems Engineering, School of Engineering Science, Simon Fraser University, 250 – 13450 102nd Avenue, Surrey, BC, Canada V3T 0A3*

(Received in Final Form: July 23, 2009. First published online: August 27, 2009)

SUMMARY
In this paper, the dynamics and biomimetic control of an artificial finger joint actuated by two opposing one-way shape memory alloy (SMA) muscle wires that are configured in a double spring-biased agonist–antagonist fashion is presented. This actuation system, which was described in Part I, forms the basis for biomimetic tendon-driven flexion/extension and abduction/adduction of the artificial finger. The work presented in this paper centres on thermomechanical modelling of the SMA wire, including both major and minor hysteresis loops in the phase transformation model, and co-operative control strategy of the agonist–antagonist muscle pair using a pulse-width-modulated proportional-integral-derivation (PWM–PID) controller. Parametric analysis and identification are carried out based on both simulation and experimental results. The performance advantage of the proposed co-operative control is shown using the metacarpophalangeal joint of the artificial finger.

KEYWORDS: Artificial finger; Artificial muscle; Shape memory alloy; Phase transformation; Hysteresis; PID; Biomimetic control.

1. Introduction

In Part I,[1] a companion paper, we introduced a new biomimetic tendon-driven actuation system for powered orthotic and prosthetic hand applications in rehabilitation robotics. The proposed actuation system is based on the combination of compliant tendon cables and one-way shape memory alloy (SMA) wires that form a set of agonist–antagonist (or so-called differential-type) artificial muscle pairs for the flexion/extension or abduction/adduction of an artificial finger joint. The design and preliminary evaluation of the proposed actuation system was carried out using an artificial finger testbed shown in Fig. 1, which was also developed based on a biomimetic design approach.[1] The artificial finger is a 4 degree-of-freedom system that consists of active flexion/extension and abduction/adduction of the metacarpophalangeal (MCP) joint, active flexion/extension of the proximal interphalangeal (PIP) joint and passive flexion/extension of the distal interphalangeal (DIP) joint. Here, in Part II, we present the modelling and co-operative closed-loop control of the proposed compliant agonist–antagonist SMA muscle pairs, focusing on the flexion/extension of the MCP joint for an in-depth representation. As a result of implementing the proposed co-operative agonist–antagonist controller, biomimetic control of the artificial finger's MCP joint is achieved.

* Corresponding author. E-mail: ed_park@sfu.ca

1.1. Overview of the proposed tendon-driven actuation mechanism

In summary, the key advantage of the proposed actuation mechanism, schematically shown in Fig. 2, is that it allows compliant and bi-directional agonist–antagonist pulling motion about each artificial finger joint. This enables the emulation of the key biological features of the natural muscle-tendon arrangement in the human hand: (i) the bi-directional (flexion/extension or abduction/adduction) motion of the natural finger joints; (ii) the compliance in the joints and (iii) the nominal resting (i.e. unactuated) state of the natural finger, which is shown in Fig. 1(a). Referring to Fig. 2, one end of each tendon cable is attached to the artificial finger structure, mimicking the attachment of the natural tendon to the finger bones, while the other end of the tendon cable is connected to the SMA actuator (from Miga Motors Company). The actuators are placed remotely to the finger joint, similar to the natural finger's extrinsic musculature. Joint rotation is produced by the contractile action of the two SMA actuators, placed in opposition to each other in a double spring-biased fashion. As shown in the lower inset of Fig. 2, passive compliance is introduced in the tendon cables of the artificial finger by connecting a spring in parallel to a slack portion of each tendon cable such that, as the SMA actuator contracts, the spring in the corresponding tendon elongates until the slack is absorbed and the tendon is taut. At this point, the tendon can be considered to have 'infinite' stiffness and further SMA actuator contraction causes tension to be transferred to the finger for link rotation. This simple spring-slack artificial tendon effectively mimics the nonlinear stiffness of the natural tendon whose stiffness tends to a larger value as it approaches its natural limit of extension. The dual spring-biased configuration permits the two opposed SMA

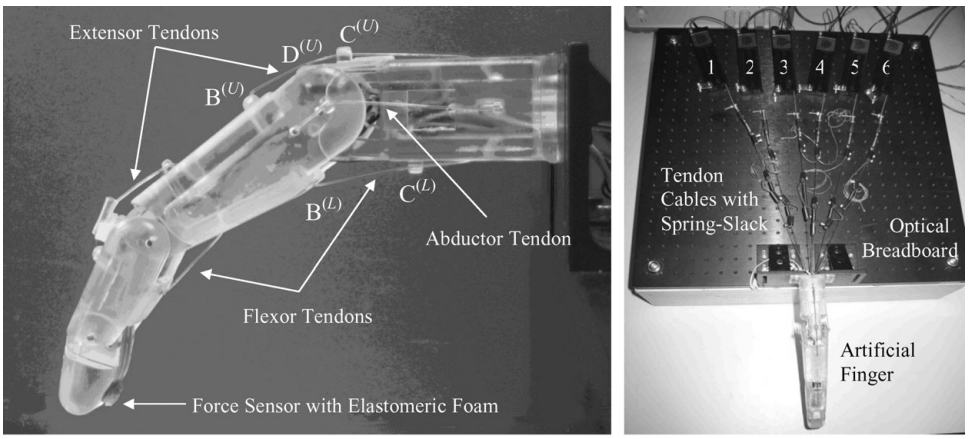

(a) Artificial finger prototype constructed using SLA-3500 RP machine loaded with Vantico CibaTool SL5510 resin.

(b) Artificial finger and six SMAs mounted on optical breadboard

Fig. 1. Artificial finger testbed with six tendon cables routing through the finger core and attached to the corresponding six remotely placed SMA actuators: (a) artificial finger prototype constructed using SLA-3500 RP machine loaded with Vantico CibaTool SL5510 resin; (b) artificial finger and six SMAs mounted on optical breadboard.

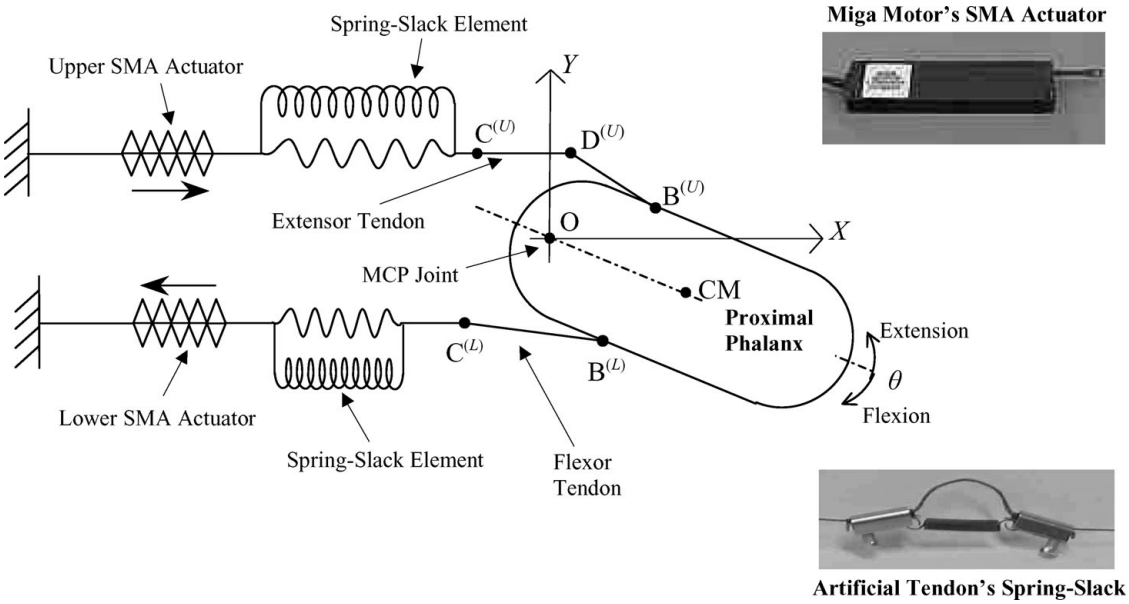

Fig. 2. Differential double spring-biased SMA actuation mechanism at the MCP joint. The insets show the actual SMA actuator and spring-slack element used.

actuators to work as an agonist–antagonist pair, enabling both active flexion and extension of the joint.

1.2. Literature survey

SMAs are metallic alloys, typically composed of nickel and titanium (Ni-Ti or nitinol), that exhibit the ability to return to a predefined shape and size when heated above a threshold temperature that is referred to as the phase transformation temperature.[2,3] This phenomenon is known as the shape memory effect and is the result of a change in the material's crystalline structure between two temperature-dependent phases: martensite and austenite. Martensite is the low temperature phase when the alloy is relatively soft and malleable, whereas austenite is the high temperature phase where the alloy is hard. One-way SMA actuators (e.g. pulling types) are available as pre-strained (i.e. trained to remember a shorter than actual length) martensitic wires. Heating beyond the transition temperature triggers the phase transformation to austenite and the wire contracts to the pre-stained length, thus exerting a pulling force that can be used for actuation. The one-way SMA actuator is usually employed in a bias type configuration, i.e. together with a bias spring for reverse actuation.[1,4–6] The main problem behind this configuration is that it can act very slowly if there is an overshoot, thus requiring active cooling. The two-way actuators, also called differential type, are composed of two SMA elements. This configuration has the advantage of easier and faster control, but requires more power, as well as increased complexity of the system.[6,7–9] SMAs can be used in direct-drive configuration eliminating the need for complex transmission systems. Furthermore,

https://doi.org/10.1017/S0263574709990324 Published online by Cambridge University Press

they possess a high power to weight ratio enabling the design of compact, lightweight systems without too much compromising power capabilities. Moreover, SMAs only use the phase transformation for actuation, which permits silent operation. However, actuation rates are dependent on the cooling capacity of the SMA wire, which ultimately limits the actuator bandwidth. Other limitations are: limited life cycle, nonlinear operation owing to hysteretic behaviour and still low actuation strains.[1]

In literature, both the one-way and two-way SMA wires have been proposed as actuators not just for dexterous hand and finger design,[1] but also for a number of other applications, e.g. vibration control,[6,10] payload lifting,[11] position control,[5,8,12,13] and beam bending.[7,9] The modelling of the nonlinear multi-physics system representing a SMA actuator can be a challenging work, since it requires the derivation of the stress–strain model of the SMA wire, the transformation model between the martensite and austenite phases, and the heat transfer model between the wire and the surrounding environment. Furthermore, since the SMA actuator is usually part of a larger mechanical system, the overall system dynamic model required for control synthesis can be very complex.

The SMA constitutive model defines the thermomechanical characteristics of the material. Since the mechanical behaviour of the SMA wire strongly depends on the phase transformation with respect to the temperature, it is not possible to use the standard stress–strain relationships. Two families of thermomechanical models can be employed: a micromechanical model or a macromechanical model.[14,15] In the former case, the models are obtained analysing the molecular behaviour, while in the latter case the models are defined using a phenomenological approach. Macromechanical models are the ones that have been most used in technological applications since they are easier to physically interpret and have parameters that can be obtained experimentally.[4–6,13,14–16] They are usually assumed to be a function of the stress, strain, temperature and martensite fraction. The last variable, the martensite fraction, represents the amount of martensite during the phase transformation and it is an internal variable that depends on stress and temperature. A more detailed discussion and comparison between macromechanical models can be found in.[14]

SMA's phase transformation is particularly difficult to model due to the hysteretic nature of the phenomena, i.e. the two transformations, from martensite to austenite (heating phase) and vice versa (cooling phase), are performed at different temperatures.[17,18] This cycle, when performed in full, is called the major hysteresis loop. If the material does not complete the full transformation during heating or cooling phase, a different hysteresis path within the major loop is followed. This smaller loop is called the minor hysteresis loop. As for the constitutive relationship, different models have been proposed in literature to define both the major and minor loops.[19,20] A quite common macromechanical approach is to use models with assumed phase transformation kinetics, i.e. where the martensite fraction defining the phase change is expressed as some known function of temperature and stress. Finally, the heat necessary for the martensite to austenite transformation is generated in the SMA wire via Joule effect, i.e. applying a voltage. During this phase, as well as during the austenite to martensite phase, energy is also lost by natural convection.[21]

In regards to control of SMA actuators, both linear and nonlinear controllers have been proposed in literature. It has been shown that the most effective control methods are pulse width modulation (PWM) in conjunction with some form of PID controller,[8,10,22–24] variable structure controller,[5,13] or sliding mode controller.[12,25] Other control schemes that have been applied are neuro-fuzzy logic and feedback linearization methods.[26–28]

In this paper, the modelling and control of the proposed biomimetic tendon-driven actuation system for artificial fingers is presented. As shown in Part I, its unique design feature is the integration of a compliant tendon (via a spring-slack element) to each one-way SMA muscle wires. This allows the formation of true agonist–antagonist artificial muscle pairs for the actuation of the flexion/extension and abduction/adduction of the metacarpophalangeal (MCP) joint and the flexion/extension of the proximal interphalangeal (PIP) joint of the artificial finger. As a result, the proposed actuation system produces similar manipulative and functional abilities found in the natural finger (refer to Part I). The main contributions of Part II are the modelling of the compliant SMA muscle wires in the agonist–antagonist configuration, and their co-ordinated actuation control. The thermomechanical properties of the wires are described using the macromechanical model proposed by Tanaka,[16] which was later expanded by Liang and Rogers.[4,6] The major and minor hysteresis loops are described using a cosinusoidal function.[4,6,13,19] The heat transfer model accounts for the Joule effect, and includes a second-order temperature dependent term representing the natural convection. The co-ordinated closed-loop control of the agonist–antagonist SMA muscle pair is performed using a PWM–PID controller. Parametric analysis and identification are carried out based on both numerical and experimental results. The performance advantage of the proposed co-operative control of the agonist–antagonist muscle pair over independent, sequential control of each muscle is verified experimentally using the MCP joint of the artificial finger.

2. Model

This section presents the modelling of the proposed biomimetic tendon-driven actuation system. The formulation is shown based on the flexion/extension of the MCP joint, accounting for the two opposing one-way SMA actuators and their spring-slack tendons (Fig. 2).

The inertial reference frame is given by the frame O-*XY* in Fig. 2, with *Y*-axis in the opposite direction of the gravitational acceleration g and *X*-axis along the horizontal direction. The resulting finger motion is in the *X*–*Y* plane and is fully defined by the angular rotation θ. Superscripts U and L are used to define quantities associated with the upper and the lower SMA actuators, respectively. In Fig. 2, the point B, which moves with respect to the MCP joint centre O, represents the attachment point between the tendons and finger structure; the points C and D along the tendons are fixed points in space with respect to the MCP joint, and

https://doi.org/10.1017/S0263574709990324 Published online by Cambridge University Press

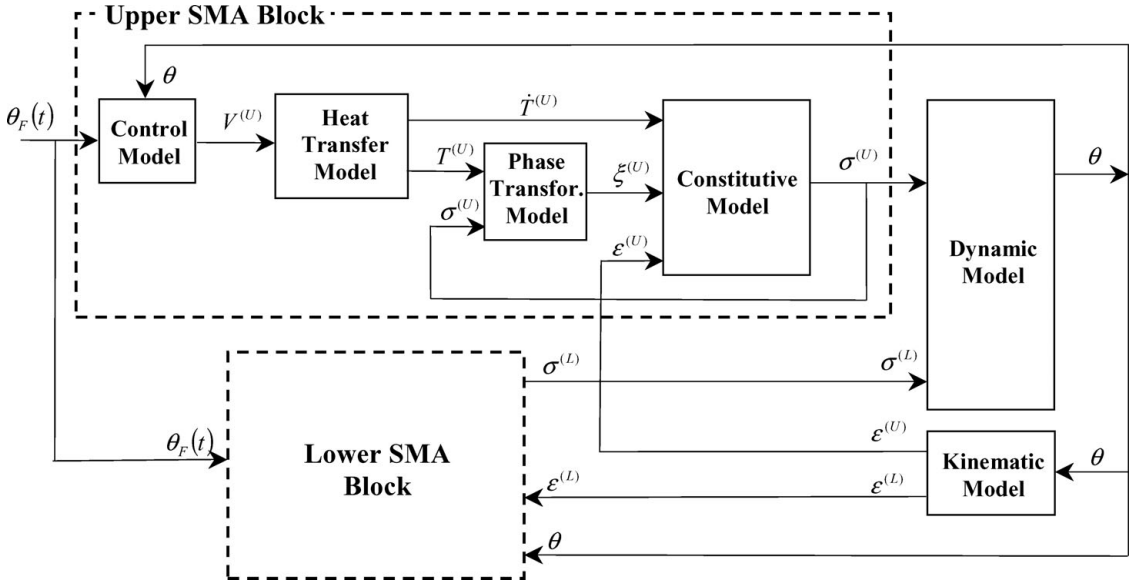

Fig. 3. Schematic representation of the overall mathematical model of the system.

they are used as the reference points for determining the deformation (i.e. contraction and elongation) of each tendon. Note that the exact location of Point D is where the tendons actually bend around the exoskeletal structure of the phalanx. Finally, the point CM represents the location of the phalanx's centre of mass.

Figure 3 and Table I show, respectively, the block diagram and symbolic representations of the equations involved in the overall mathematical model of the system where: σ is the stress, ε is the total strain, T is the temperature, ξ is the martensite fraction, V is the applied voltage and $\theta_F(t)$ is the desired (or final) angular position of the joint. The lower SMA block in Fig. 3 is structured exactly the same as the upper SMA block, and its details are excluded for the simplicity of the diagram. In the subsequent sections, the governing equations behind each block are explained.

In summary, the overall model is represented by a system of coupled (nonlinear) ordinary differential equations (shown in Table I) that has been solved using an explicit fixed-step solver (ODE45 in Matlab/Simulink) with a small time step in the range of 0.01–0.1 ms.

2.1. Dynamic model

Figure 4 shows a schematic representation of the external forces acting on the proximal phalanx.

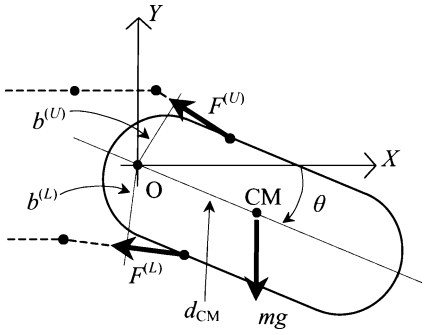

Fig. 4. External forces acting on the proximal phalanx.

The equations of motion can be given by:

$$I\ddot{\theta} = M_E - M_{Fr}, \tag{1a}$$

$$M_E = F^{(U)}b^{(U)} - F^{(L)}b^{(L)} - \mathrm{mgd}_{CM}\cos\theta \tag{1b}$$

in which $F^{(U)} = \sigma^{(U)}S_w$ and $F^{(L)} = \sigma^{(L)}S_w$. In the above equations, I and m are the phalanx' moment of inertia (about the Z-axis) and mass, respectively; M_E represents the total external moment acting on the structure, while M_{Fr} represents the frictional moment in the MCP joint. The two forces, $F^{(U)}$ and $F^{(L)}$, in Eq. (1b) are determined from the

Table I. Symbolic equations of the overall mathematical model.

Model	Symbolic form	Equations
Dynamic	$\ddot{\theta} = f\left(\theta, \dot{\theta}, \sigma^{(U)}, \sigma^{(L)}\right)$	(1)–(2)
Kinematic	$\varepsilon^{(U)} = f(\theta); \varepsilon^{(L)} = f(\theta)$	(3)–(6)
Constitutive	$\dot{\sigma}^{(U)} = f\left(\dot{\varepsilon}^{(U)}, \dot{T}^{(U)}, \dot{\xi}^{(U)}\right); \dot{\sigma}^{(L)} = f\left(\dot{\varepsilon}^{(L)}, \dot{T}^{(L)}, \dot{\xi}^{(L)}\right)$	(7)–(8)
Phase transfer	$\dot{\xi}^{(U)} = f\left(\sigma^{(U)}, T^{(U)}\right); \dot{\xi}^{(L)} = f\left(\sigma^{(L)}, T^{(L)}\right)$	(9)–(10)
Heat transfer	$\dot{T}^{(U)} = f\left(T^{(U)}, V^{(U)}\right); \dot{T}^{(L)} = f\left(T^{(L)}, V^{(L)}\right)$	(11)
Control	$V^{(U)} = f\left(\theta, \dot{\theta}, \ddot{\theta}\right); V^{(L)} = f\left(\theta, \dot{\theta}, \ddot{\theta}\right)$	(12)

https://doi.org/10.1017/S0263574709990324 Published online by Cambridge University Press

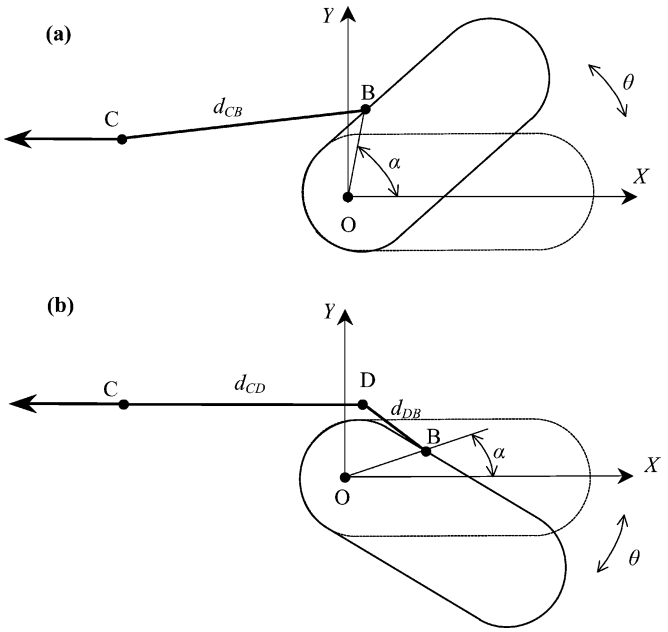

Fig. 5. Geometric illustration of (a) Configuration I and (b) Configuration II.

corresponding stresses $\sigma^{(U)}$ and $\sigma^{(L)}$, and are applied along the tendon at the attachment points $B^{(U)}$ and $B^{(L)}$, with b being the normal distance between the tendon and the MCP joint centre. The term d_{CM} defines the distance between the centre of mass CM and the MCP joint centre O, and S_w is the SMA muscle wire's cross-sectional area. Finally, the frictional moment, M_{Fr}, is modelled using the Coulomb-viscous model,[29] i.e.

$$\begin{array}{lll} M_{Fr} = \text{sign}(\dot{\theta})(M_{DF} + C_{DF}|\dot{\theta}|) & \text{if} & |M_E| > M_{SF} \\ M_{Fr} = M_E & \text{if} & |M_E| \leq M_{SF} \end{array}, \tag{2}$$

where M_{DF} is the dynamic friction moment, C_{DF} is the dynamic friction coefficient and M_{SF} is the static friction moment.

2.2. Kinematic model

The kinematic model relates the change in the rotary position of the proximal phalanx θ, from its initial configuration to the total strain variation $\Delta\varepsilon$. This strain variation is due to the elastic deformation in the tendon cable and in the SMA wire, and the deformation associated with the phase transformation in the SMA wire. Furthermore, we assume that the deformation in the tendon cable is due to the spring-slack element only. At any given instant each actuator can only be in one of two configurations, Configurations I and II, which are illustrated in Figs. 5(a) and 5(b), respectively. Since the kinematic relationships in both configurations are independent of the choice of the upper or lower SMA actuators, the superscripts U and L are omitted and the upper SMA actuator is used as a representative case.

Configuration I. In Fig. 5(a), the upper tendon is contracting, and the proximal phalanx is undergoing extension. In this particular case, the upper tendon does not touch the exoskeletal structure of the phalanx, i.e. Point D is absent (refer to Fig. 2). Point C, which is a fixed coordinate (X_C, Y_C) in the inertial frame O-XY, is used as the reference point for determining the total strain variation $\Delta\varepsilon$. Thus, the coordinates for Point B are given by

$$\begin{cases} X_B = r\cos(\alpha) \\ Y_B = r\sin(\alpha) \end{cases}, \tag{3}$$

where r is the distance between Points B and O, and α is the angle defining the position of Point B. This angle is related to the finger rotation, i.e. $\alpha = (\theta + \alpha_0)$, where α_0 is a constant and it is the value of α corresponding to the initial configuration, i.e. for $\theta = 0$. The total strain variation $\Delta\varepsilon$ due to a rotation of the phalanx is given by

$$\Delta\varepsilon = \frac{(d_{CB} - d_{CB0})}{L_w} \tag{4a}$$

in which $d_{CB} = \sqrt{(X_B - X_C)^2 + (Y_B - Y_C)^2}$ and L_w is the unstretched length of the SMA wire. Term d_{CB0} represents d_{CB} in the initial configuration, i.e. when $\theta = 0$. The force arm b is the altitude of the triangle OCB where the segment CB is the base; thus, it can be determined from the area of the triangle OCB, i.e.

$$A_{OCB} = \frac{1}{2}|\mathbf{P}_{OB} \times \mathbf{P}_{OC}| = \frac{1}{2}|X_B Y_C - X_C Y_B| = \frac{1}{2} d_{CB} b$$
$$\text{or } b = \frac{|X_B Y_C - X_C Y_B|}{d_{CB}}, \tag{4b}$$

where $\mathbf{P}$ is the distance vector between the two points indicated by the corresponding subscripts.

Configuration II. In Fig. 5(b) the upper tendon is stretching (i.e. the lower tendon is contracting), and the proximal phalanx is undergoing flexion. In opposite to the previous case, here the upper tendon has another contact point (on top of C and B) on the phalanx: Point D, which is defined by the fixed coordinates (X_D, Y_D). All the other points and distances have the same meaning as in the previous configuration. The resulting kinematic relationship is then as follows:

$$\Delta\varepsilon = \frac{(d_{DB} - d_{DB0})}{L_w} \tag{5a}$$

in which $d_{DB} = \sqrt{(X_B - X_D)^2 + (Y_B - Y_D)^2}$. As before, the term d_{DB0} represents d_{DB} in the initial configuration, i.e. for $\theta = 0$, and the force arm b can be determined from the area of the triangle ODB:

$$A_{ODB} = \frac{1}{2}|\mathbf{P}_{OB} \times \mathbf{P}_{OD}| = \frac{1}{2}|X_B Y_D - X_D Y_B| = \frac{1}{2} d_{DB} b$$
$$\text{or } b = \frac{|X_B Y_D - X_D Y_B|}{d_{DB}}. \tag{5b}$$

Now, the variation in the total strain, $\Delta\varepsilon$, is related to the total strain ε by

$$\Delta\varepsilon = \varepsilon + \varepsilon_0 \tag{6}$$

https://doi.org/10.1017/S0263574709990324 Published online by Cambridge University Press

where $\varepsilon = \varepsilon_s + \varepsilon_e + \varepsilon_t$ and ε_0, is the strain corresponding to the initial configuration. The total strain is composed by the strain due to the spring ε_s, the strain due to the SMA wire elasticity ε_e and the strain due to the SMA wire phase transformation ε_t.

2.3. SMA constitutive model

The SMA constitutive model defines the thermomechanical characteristics of the material – i.e. the effect of the temperature on the stress as the SMA undergoes phase transformation. We adopted the model proposed in,[4,6,16] since it has been proven to describe the phenomena quite accurately. The relationship relating stress σ, strain ε, temperature T and martensite fraction ξ for the SMA wire can be written in the following differential form

$$\dot{\sigma} = D\left(\dot{\varepsilon}_e + \dot{\varepsilon}_t\right) + \theta_T \dot{T} + \Omega\dot{\xi}, \tag{7a}$$

where $D = D_A + \xi(D_M - D_A)$ and $\Omega = -\varepsilon_R D$, $\varepsilon_t = \xi\varepsilon_R$. D_A and D_M are the austenite and martensite Young's modulus, respectively; θ_T is the thermo-elastic factor; Ω is the phase transformation contribution factor and ε_R is the maximum strain that can be recovered through the transformation phase. The actual Young's modulus D is thus assumed to change linearly between the martensite and austenite values D_A and D_M. The martensite fraction is not an independent variable, and will be defined later in Section 2.4. Note that Eq. (7a) can be rewritten as

$$\dot{\sigma} = D\dot{\varepsilon}_t + D_{eq}\left(\dot{\varepsilon}_e + \dot{\varepsilon}_s\right) + \theta_T \dot{T} + \Omega\dot{\xi}, \tag{7b}$$

where the term D_{eq} represents the equivalent Young's modulus of the combined SMA wire and spring in the system. If K_s denotes the spring constant, this term can be determined as[29]

$$D_{eq} = \frac{K_s}{K_D + K_s} D = K_{eq}\frac{L_w}{S_w}, \tag{8}$$

where $K_D = DS_w/L_w$ is the equivalent spring constant of the SMA wire, and K_{eq} is the equivalent spring constant of the SMA wire spring. To take into account the effects of the slack element, a penalty term is added to K_s, so that its value tends to a larger value (following a hyperbolic cosine profile) when the spring length reaches the slack length.

2.4. SMA phase transformation model

The phase transformation model relates the martensite fraction ξ to the temperature T and the stress σ. Following a common and well verified approach in literature, we will assume in priori the function representing the heating and cooling phases. This function differs for the two phases, so to include the hysteresis effects of the phenomena, but both are represented by a cosinusoidal term.[5,6,13,19]

2.4.1. Heating phase

$$A_S = A_{S0} + \sigma/c_A \text{ and } A_F = A_{F0} + \sigma/c_A$$

$$\text{where } \begin{cases} 1 & T < A_S \\ \xi & A_S \le T \le A_F, \\ 0 & T > A_F \end{cases} \tag{9a}$$

$$\xi = \frac{\xi_{M0}}{2}\left\{\cos\left[a_A\left(T - A_{S0}\right) + b_A\sigma\right] + 1\right\}$$

$$\text{where } a_A = \pi/\left(A_{F0} - A_{S0}\right),\ b_A = -a_A/c_A. \tag{9b}$$

In Eq. (9), A_S and A_F are the austenite phase start and final temperatures; ξ_{M0} is the martensite fraction at the beginning of the phase (equal to the amount of martensite fraction at the end of the previous cooling phase); A_{S0} and A_{F0} are, respectively, the austenite phase start and final temperatures for zero stress; c_A is the austenic material coefficient.

2.4.2. Cooling phase

$$M_S = M_{S0} + \sigma/c_M \text{ and } M_F = M_{F0} + \sigma/c_M$$

$$\text{where } \begin{cases} 1 & T < M_F \\ \xi & M_F \le T \le M_S, \\ 0 & T > M_S \end{cases} \tag{10a}$$

$$\xi = \frac{1 - \xi_{A0}}{2}\cos\left[a_M\left(T - M_{F0}\right) + b_M\sigma\right] + \frac{1 + \xi_{A0}}{2}$$

$$\text{where } a_M = \pi/\left(M_{F0} - M_{S0}\right),\ b_M = -a_M/c_M. \tag{10b}$$

In Eq. (10), M_S and M_F are the martensite phase start and final temperatures; ξ_{A0} is the martensite fraction at the beginning of the phase (equal to the amount of martensite fraction at the end of the previous heating phase); M_{S0} and M_{F0} are, respectively, the martensite phase start and final temperatures for zero stress; c_M is the martensitic material coefficient.

While for a major hysteresis loop ξ_{M0} is always equal to one and ξ_{A0} is always equal to zero, for a minor hysteresis loop those two terms are assumed to be equal to the last value of martensite fraction reached during the previous phase. In reality, the thermodynamic behaviour of the material during minor hysteresis loops is much more complicated,[17–19] but for our application this assumption produced satisfactory results. Note that the start and final temperatures of each phase is also correctly defined as a function of the wire stress.

2.5. Heat transfer model

The heat necessary for the martensite to austenite transformation is generated applying a voltage to the SMA wire. Part of the energy generated by this electric field goes into actually increasing the wire temperature, while the remaining part is lost by natural convection. Such a thermal model can be represented by the following equation:[21]

$$M_w C_p \dot{T} = \frac{V^2}{R_w} - hA_w\left(T - T_{\text{amb}}\right), \tag{11}$$

where M_w is the mass per unit length; C_p is the specific heat; V is the applied voltage; R_w is the electrical resistance per unit length; h is the heat convection coefficient, assumed be a quadratic function of the temperature with parameters h_0 and h_2, i.e. $h = h_0 + h_2T^2$; A_w is the wire circumferential area and T_{amb} is the ambient temperature. The specific heat and resistance are treated as constants, neglecting their dependency on the temperature.[18]

https://doi.org/10.1017/S0263574709990324 Published online by Cambridge University Press

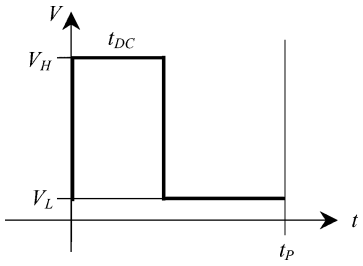

Fig. 6. Pulse-width-modulation scheme.

2.6. Control procedure

As shown in Fig. 6, the heating/cooling phases can be controlled by switching the voltage in the wires between V_H and V_L, and changing the duty cycle, t_{DC}, within the fixed time period t_P. For practical purposes V_L is assumed to be zero. Then a PWM–PID controller[8,10,22–24] is employed, which relates the angular information of the finger to the duty cycle, expressed in percent, i.e.

$$DC_{\%} = K_P \Delta\theta + K_V \Delta\dot{\theta} + K_I \int \Delta\theta \, \mathrm{d}t, \qquad (12a)$$

$$t_{DC} = \frac{t_P DC_{\%}}{100}, \qquad (12b)$$

where $\Delta\theta = \theta_F(t) - \theta$ with the parameters K_P, K_V and K_I, being the proportional, derivative and integral gains, respectively. The value of $DC_{\%}$ is always between 0 and 100, which results in the voltage in the wire being modulated between V_H and V_L inside the period t_P, generating a PWM control signal based on a set reference value (e.g. a desired joint position angle θ_F).

Then, we implemented and compared two control strategies. In the first strategy only one actuator, namely the 'agonist actuator', is actively used to perform the requested finger rotation. Here the second actuator, namely the 'antagonist actuator', is used just as a passive bias spring. In the second strategy, the antagonist actuator is also actively used when the agonist actuator is in the cooling phase, thus hypothetically producing a faster and more robust joint motion. With the active use of both actuators, it is also possible to overcome additional problems such as parameter uncertainties and unmodelled dynamics. Note that when two actuators are used together in the proposed true agonist–antagonist fashion, particular attention has to be made to avoid a situation where both actuators are in the heating phase simultaneously, which may result in the rupture of the wires. In both strategies, the phase is determined by comparing the finger's desired joint position θ_F, with the finger's actual joint position θ. Thus, if the finger's desired rotation is positive, the agonist actuator (the upper actuator) will be in the heating phase when $\theta_F \geq \theta$ and in the cooling phase when $\theta_F < \theta$, while the antagonist actuator (the lower actuator) will be in the heating phase when $\theta_F \leq \theta$ and in the cooling phase when $\theta_F > \theta$. If the finger's desired rotation is negative, the agonist actuator (the lower actuator) will be in the heating phase when $\theta_F \leq \theta$ and in the cooling phase when $\theta_F > \theta$, while the antagonist actuator (the upper actuator) will be in the heating phase when $\theta_F \geq \theta$ and in the cooling phase when $\theta_F < \theta$.

Table II. System parameters used for numerical simulations.

Parameter	Value	Parameter	Value
ρ_w	6450 kg/m^3	L_w	0.385 m
d_w	0.375×10^{-3} m	M_{SF}	0.01 Nm
C_p	322 J/kg°C	M_{DF}	0 Nm
R_w	8.6 Ωm	C_{DF}	0.02
T_{amb}	23°C	K_P	0 rad^{-1}
A_{S0}	75°C	K_V	0 s/rad
A_{F0}	110°C	K_I	0 s^{-1}rad^{-1}
c_A	10.3×10^6 Pa/°C	I	4.88×10^{-5} kgm^2
M_{S0}	85°C	M	1.5×10^{-2} kg
M_{F0}	60°C	d_{CM}	0.035 m
c_M	10.3×10^6 Pa	V_H	8 V
D_A	75×10^9 Pa	V_L	0 V
D_M	28×10^9 Pa	t_P	1/1000 s
ε_R	2.3%	h_0	70
K_S	140 N/m	h_2	0.001

3. Parameter Analysis and Identification

A numerical code was developed in MATLAB/Simulink to simulate the MCP joint motion of the artificial finger system and to carry out a parametric analysis. The latter is performed to identify some of the system parameters, including the gains for the proposed control strategies. Table II shows the main parameters of the system. The SMA wire parameters were taken in part from specifications given by the manufacturer (Miga Motors Company) and in part from literature, while the artificial finger's geometric parameters were directly measured from the actual model shown in Fig. 1. The thermoelastic factor θ_T was assumed to be zero because any thermal expansion of the SMA wire does not actually generate any length variation in the wire. This is due to the particular design of the Miga Motors SMA actuators.

3.1. Parametric analysis

The benchmark case for the parametric analysis, which involves the flexion and extension of the MCP as a representative joint, employs the parameters given in Table II. The initial MCP joint position of the finger is at -40° and initial lengths of the upper and lower spring are at 17.4 mm and 15.5 mm, respectively. For both springs, the slack element becomes active after an elongation of 7 mm from the corresponding initial lengths. Open-loop control was used for parametric analysis by applying a constant voltage (V_H) of 8 V until the MCP joint reached its maximum possible angular range, and then removing the voltage to move the finger back to its initial position. Several parameters were varied at one at a time, including the friction coefficients, applied voltages, heat convection coefficients and the initial lengths of the two springs. Simulations showed that the system is particularly sensitive to the parameters defining the friction model and the heat convection model. Some of the results that are related to these two parameters are illustrated next.

Figure 7 shows the results of changing the coefficient of dynamic friction C_{DF} in Eq. (2). As expected, this parameter influences mainly how quickly the finger can reach a desired position. The static friction torque M_{SF} was important in determining the initial slope of the heating phase, as well as

https://doi.org/10.1017/S0263574709990324 Published online by Cambridge University Press

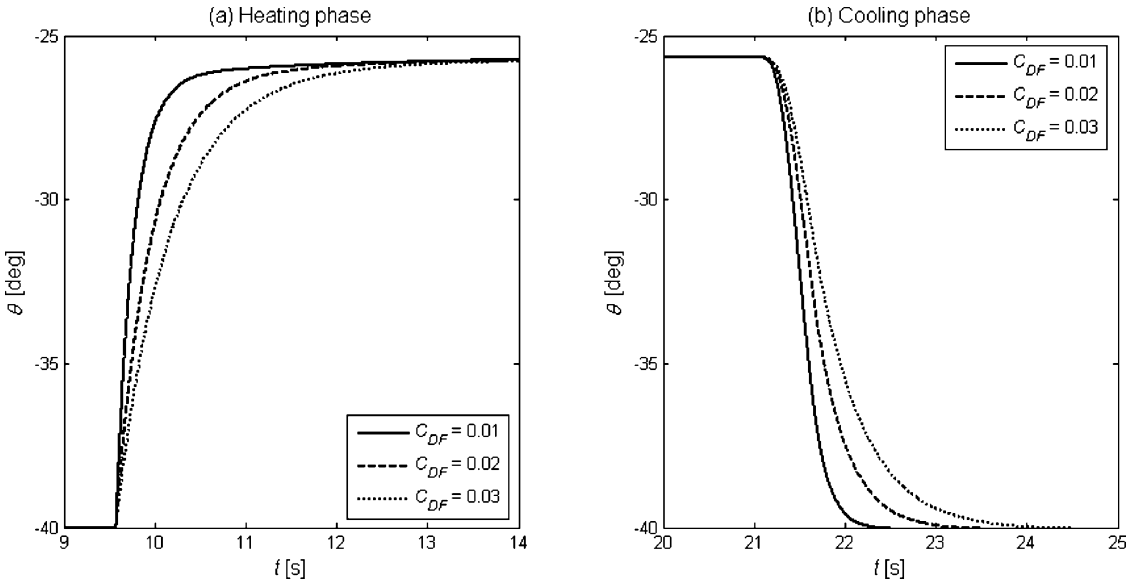

Fig. 7. Results of changing the coefficient of dynamic friction C_{DF} for (a) heating phase and (b) cooling phase.

the delay in the start of the joint motion. Note that, in order to simplify the friction model, any stick–slip effects were neglected and we assumed that $M_{DF} = 0$, i.e. the friction is purely viscous after the onset of the motion.

Figure 8 shows the results of changing the coefficient h_0 in the heat convection model given by Eq. (11). During the heating phase, this coefficient determines not only the range of motion, i.e. the maximum angular rotation attainable, but also how quickly the SMA reaches the transition phase, thus how quickly the joint starts to rotate. Since the heat convection model represents lost heat, lower the value of h_0 the better was the performance – (see Fig. 8(a)). The cooling phase plots in Fig. 8(b) was obtained using the same h_0 values (i.e. $h_0 = 60$, 65 and 70) of the heating phase. In summary, the parameter h_0 mainly affected how quickly the joint goes back to the initial position. Similar qualitative results were obtained with respect to h_2 in the same equation, but with a smaller effect on the overall performance for the considered range of temperature (20 °C 110 °C).

3.2. Parameter identification

The parametric analysis in the previous section indicated a particular dependence of the system on the friction and heat convection models. Therefore, next, experimental tests were carried out to identify the coefficients h_0, h_2 and C_{DF}. The numerical heating and cooling curves were then fitted to the corresponding experimental curves, as shown in Fig. 9. This parameter identification process yielded the following results: (i) $h_0 = 20$, $h_2 = 5 \times 10^{-4}$ and $C_{DF} = 0.03$ for the heating phase and (ii) $h_0 = 41$, $h_2 = 5 \times 10^{-4}$ and $C_{DF} = 0.09$ for the cooling phase. The remaining parameters stayed the same as given in Table II.

Since the thermal and frictional behaviour are actually different between the heating and cooling phases, a different

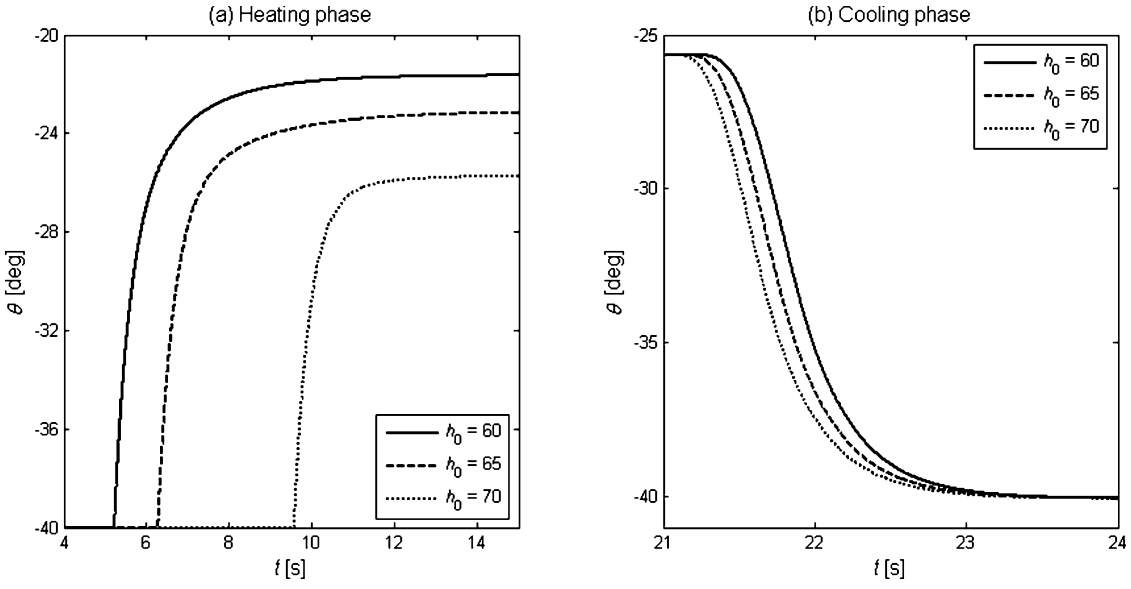

Fig. 8. Results of changing the coefficient h_0 in the heat convection model for (a) heating phase and (b) cooling phase.

https://doi.org/10.1017/S0263574709990324 Published online by Cambridge University Press

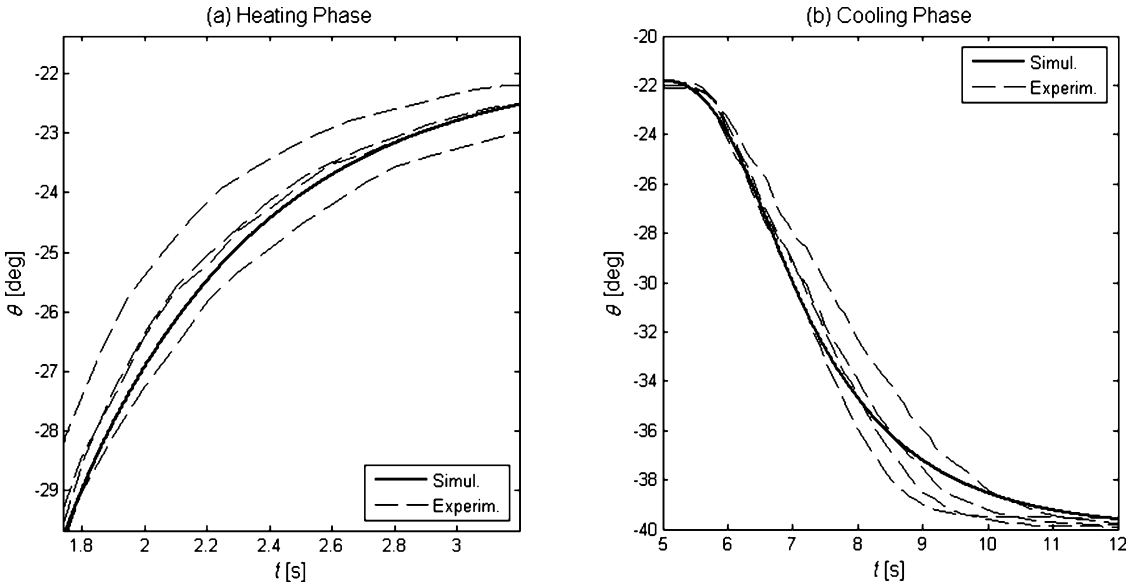

Fig. 9. Fitting of numerical simulation curves to the experimental curves for (a) heating phase and (b) cooling phase.

set of values were chosen for the above parameters. For example, during the cooling phase the thermal effects are modified by the increase in the temperature (i.e. $> T_{\text{amb}}$, the room temperature that was defined initially) around the SMA wire from the previous heating phase. This effect is further amplified by the particular design of the actuator that we employed, where the SMA wire is embedded inside a plastic casing (see Fig. 2, the upper inset) and not directly exposed into the open air, further delaying the cooling. A more accurate thermal model would include the additional modelling of the heat transfer between SMA wire and the inside air of the actuator, and then the modelling of the heat transfer between the inside air of the actuator and the open air through the casing. Figure 10(a) shows the actual temperature profile taken inside the actuator casing (proximal to the SMA wire), using a miniature fibre Bragg grating sensor. In this particular case, the actuator was turned on and off three times consecutively in an open-loop mode, with about 30 s of cool-down period between each cycle. As expected, it resulted in a stepwise increase from the initial temperature of around 23°C, with not enough time to provide complete cooling between two consecutive cycles. Figure 10(b) shows two experimental examples of irregular open-loop behaviour of the finger caused by the frictional effects. While we have lumped all friction effects (including also the friction due to the contact between the wires and the exoskeletal structure) with one 'equivalent' viscous term, represented by C_{DF}, the actual frictional behaviour may involve the phenomenon of sticking during the cooling phase – especially if the initial tension from the bias spring is chosen incorrectly. In conclusion, all these problems make the behaviour of the actuator, during cooling phase in particular, almost unpredictable.[11] One possible way to overcome these problems and improve the performance of the system is to

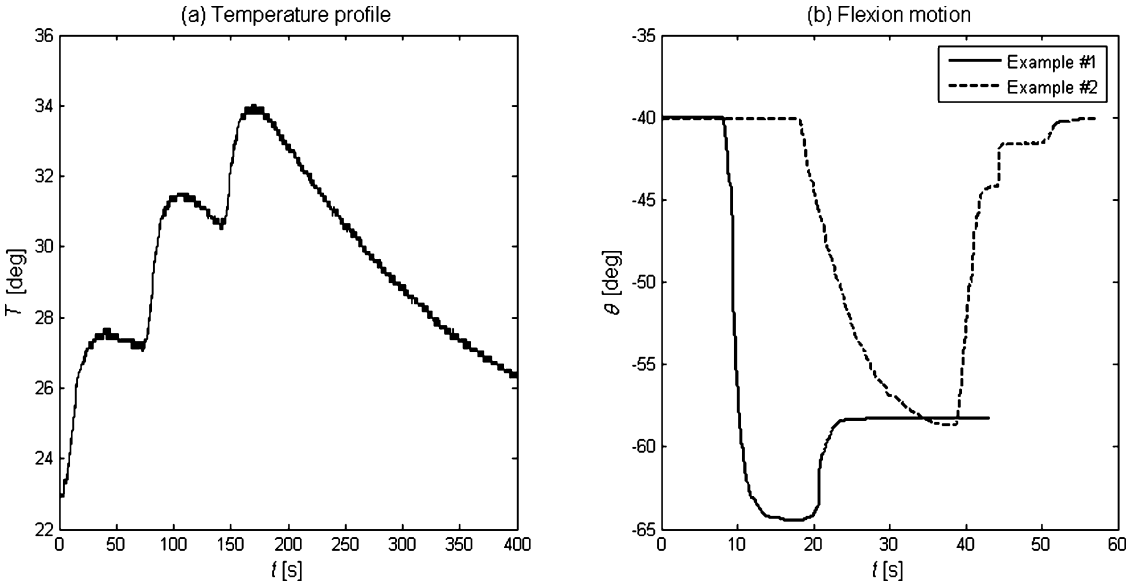

Fig. 10. Experimental examples of (a) the actual temperature profile taken inside the SMA actuator casing and (b) irregular flexion motion due to sticking phenomena.

https://doi.org/10.1017/S0263574709990324 Published online by Cambridge University Press

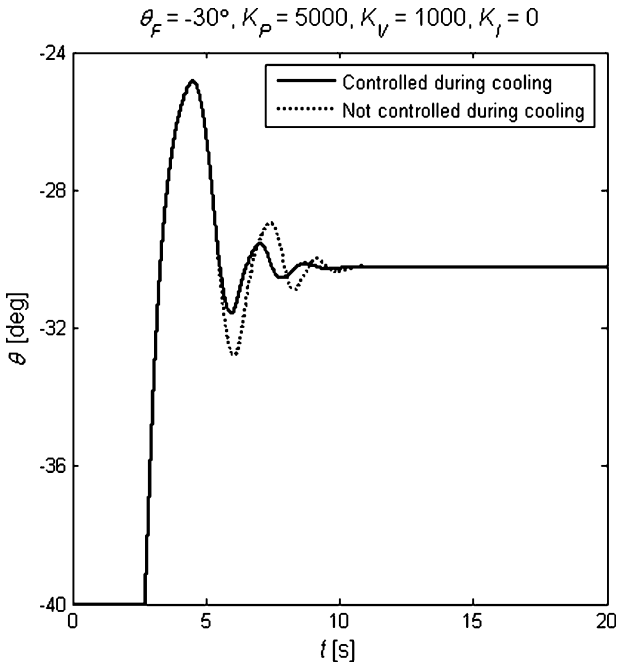

Fig. 11. Simulation results comparing between (i) controlled and (ii) uncontrolled cooling phase for the extension of the MCP joint using only the upper actuator.

use an effective closed-loop control strategy, such as the one proposed in the next section.

4. Independent versus Co-operative Agonist–Antagonist Artificial Muscle Control

4.1. Independent agonist–antagonist artificial muscle control

The first 'common' control strategy is to use one actuator (upper or lower) at a time. Once the initial position is defined (e.g., −40° MCP flexion/extension for a nominal finger position), it is possible to rotate the joint with a sequence of flexion or extension movements by using the lower or upper actuator, respectively. Here, the antagonist actuator simply works as a bias spring. Figure 11 shows simulation results of the system for an extension of the MCP joint from −40° to −30°, using the upper actuator, with the parameters identified earlier and a controller update rate of 0.01 s. Figure 11 provides a comparison of the following two cases: (i) the controller remained on during the cooling phase and (ii) the controller turned off during the cooling phase, which resulted in a relatively faster cooling but a tendency to overshoot the desired joint position.

The remainder of this section (Section 4.2) demonstrates the performance advantage of using the agonist–antagonist actuators co-operatively. Figure 12 shows a couple of simulation examples for both extension and flexion motions, with the proportional, derivative and integral gains set to 3000, 3000 and 50, respectively. While these constant gain values give a varying degree of closed-loop performance for different final flexion/extension angles (this is due to due to the nonlinear nature of the system), the deviations were small for our tested range of motion (+15°/−15°). As discussed in Part I, the actual range of the motion of the artificial finger is restricted due to the limited stroke of the Miga Motors SMA actuators (i.e. 0.5 in.), and not by the proposed actuation mechanism itself.

A full range of motion (e.g. from −25° to −55°), could be performed by first heating up the upper actuator to move the joint to −25° from the nominal position of −40° and then cooling the actuator down to move the joint back to −40°. This is followed by heating up of the lower actuator to reach −55°. This procedure would require waiting for the end of each cooling phase of the agonist actuator before activating the antagonist actuator. As shown in Fig. 12 the cooling phase can last for a significant duration (i.e. almost 10 s), reducing the overall bandwidth of the system. Furthermore, the actual cooling phase may be delayed by the sticking phenomena and the increase in the temperature inside the actuator casing, as discussed earlier in Section 3.2.

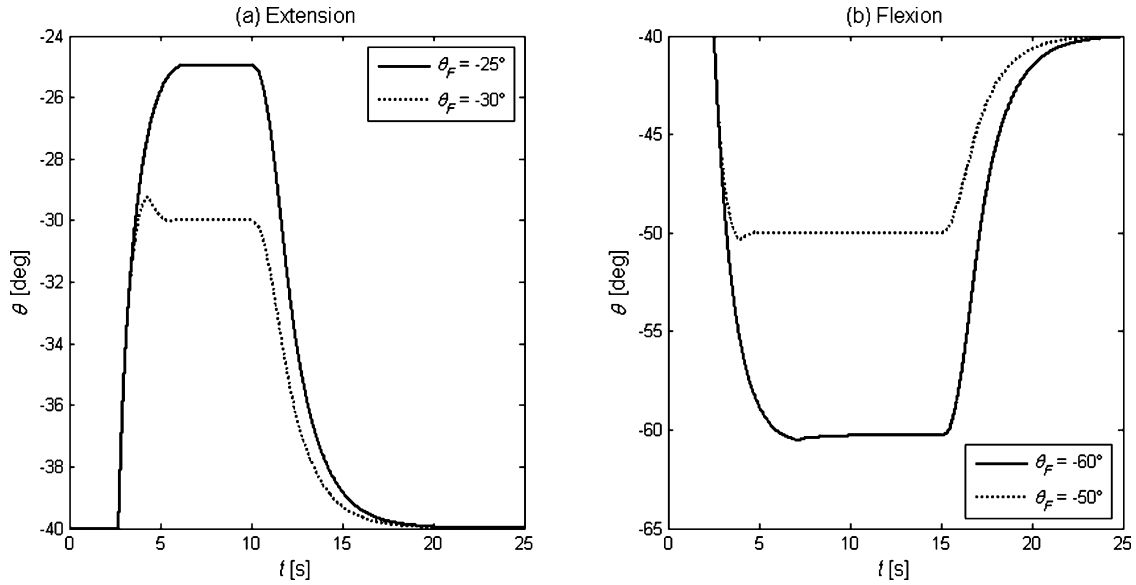

Fig. 12. Simulation examples of closed-loop rotations in (a) extension and (b) flexion using one actuator (upper and lower actuator, respectively).

https://doi.org/10.1017/S0263574709990324 Published online by Cambridge University Press

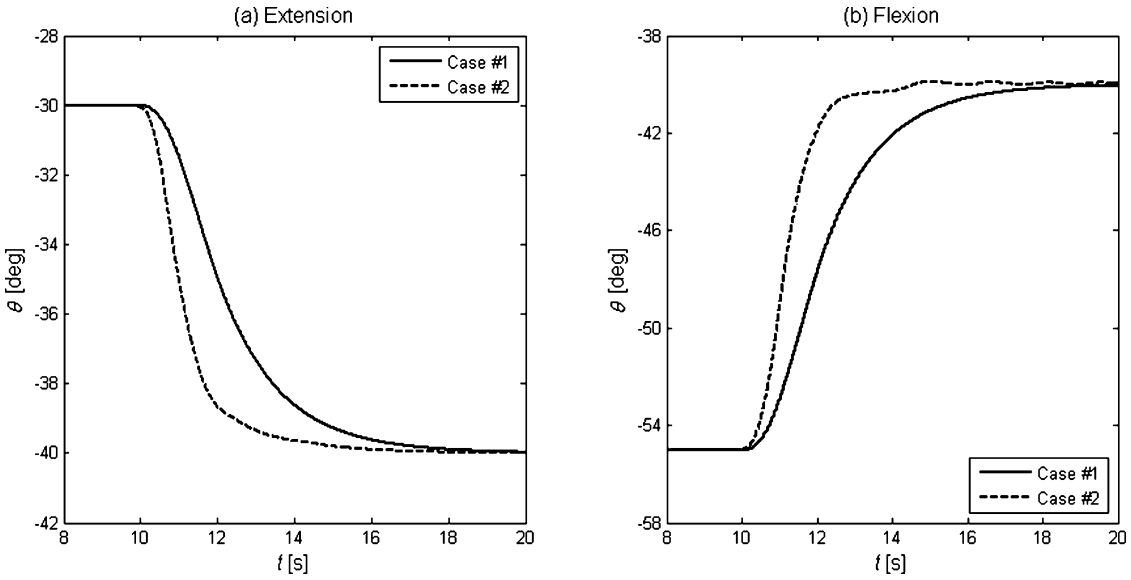

Fig. 13. Simulation examples of closed-loop control in (a) extension and (b) flexion of the MCP joint using both upper and lower actuators.

4.2. Co-operative agonist–antagonist artificial muscle control

A more effective strategy would be to actively use both agonist–antagonist actuators simultaneously, in a similar (i.e. biomimetic) way to the natural muscles. In another words, while the agonist actuator is still in the cooling phase, the antagonist actuator is also activated (i.e. enters the heating phase). As a result, this not only reduces the time for the joint to return to its initial (or nominal) position but also allows to overcome any sticking problems. Figure 13 shows the results from two simulation case studies performed for both flexion and extension motion of the MCP joint (note that in the two plots only the cooling phase is shown). In the extension cases, i.e. Fig. 13(a), the joint was rotated to -30° from the nominal position using the upper actuator, and during its cooling phase the lower actuator was also activated. In the flexion cases, i.e. Fig. 13(b), the joint was rotated to -55° using the lower actuator and the upper actuator is activated during its cooling phase. As usual, the values from Table II were used, together with the identified parameter values from Section 3.2, and the PID gains of 3000, 3000 and 50, respectively.

Case # 1 represents the situation where only the agonist actuator is used, thus no effects from the antagonist actuator is present (i.e. the same situation as in Section 4.1). Case # 2 represents the situation where the antagonist actuator is also used co-operatively. The antagonist actuator is activated just before the agonist actuator starts its cooling phase. The improved performance of Case # 2 over Case # 1 is clearly visible from Fig. 13. The effectiveness of the proposed co-operative control strategy of the agonist–antagonist artificial muscles is more evident from actual experiments performed on the artificial finger. Figure 14 shows a couple of

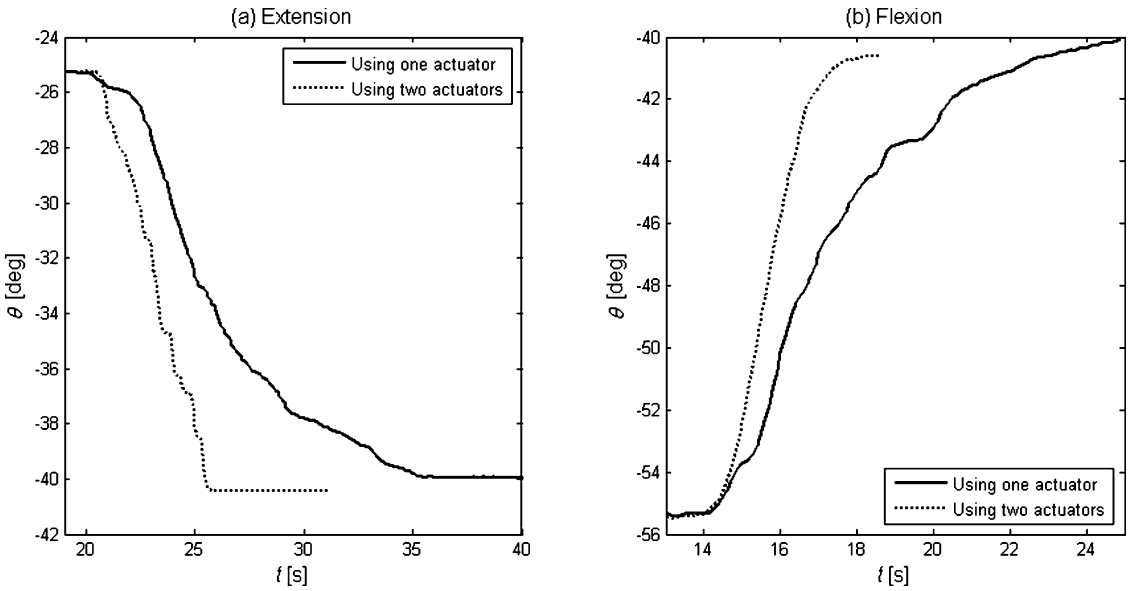

Fig. 14. Experimental examples of closed-loop control in (a) extension and (b) flexion of the MCP joint, comparing between independent and co-operative agonist–antagonist artificial muscle control.

https://doi.org/10.1017/S0263574709990324 Published online by Cambridge University Press

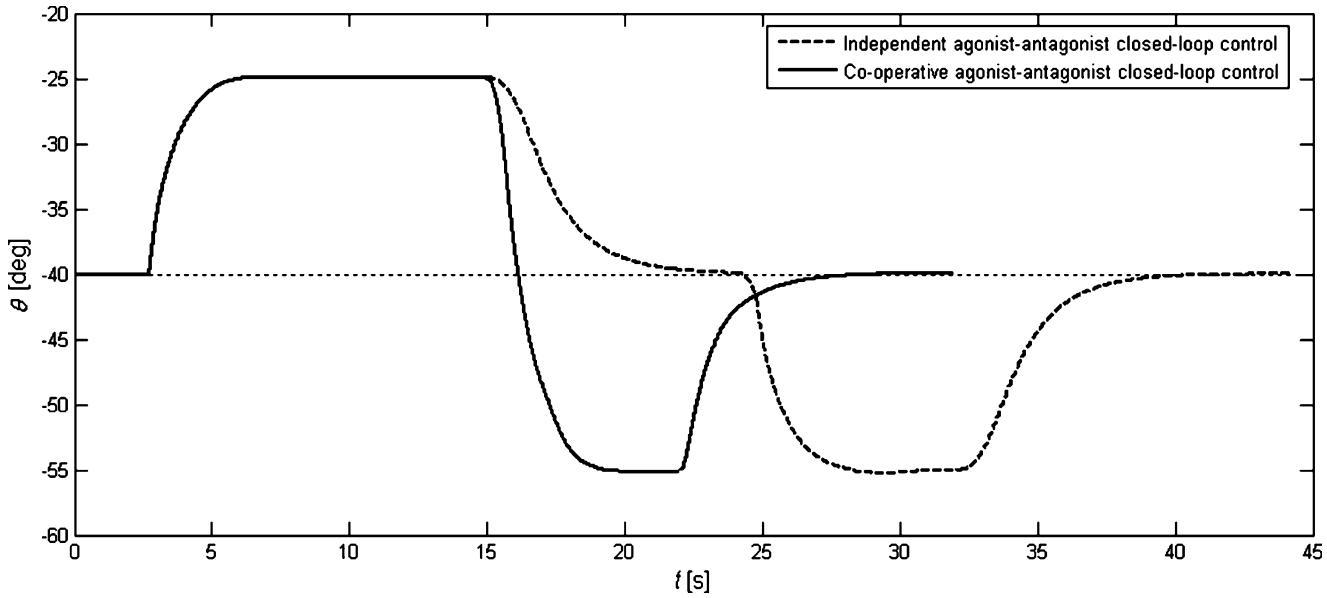

Fig. 15. Simulation example of full extension–flexion motion using (i) independent vs. (ii) co-operative agonist–antagonist artificial muscle control.

experimental examples, one for the extension and the other for the flexion of the MCP joint, the co-operative controller shaving off as much as 10 s in reaching the desired joint position.

Finally, as shown in Fig. 15, the agonist–antagonist actuator pair can also be used to co-operatively perform a full extension–flexion motion. In this simulation example, the finger first extends from the initial position of -40° to -25°, then flexes to -55° before coming back to the initial position. While the independent controller takes about 37.5 s to produce the full extension–flexion motion cycle, the co-operative controller only takes 27.5 s (a 27% reduction in time). While this is a significant reduction, still for practical implementation purposes, the actuator bandwidth needs to be further reduced. This can only be achieved with a much improved design upon the Miga Motors SMA actuators that we employed – this is our ongoing work.

5. Conclusions

The aim of this work is to develop an accurate dynamic model and an effective biomimetic controller for a novel biomimetic tendon-driven actuation system for artificial fingers. The actuation system uses two opposing SMA actuators in a double spring-biased agonist–antagonist configuration, allowing bi-direction flexion/extension or abduction/adduction of a finger joint. Accurate models for describing the thermomechanical properties, phase transformation and heat transfer of the SMA wires have been defined. An in-depth parametric analysis has been carried out to determine the critical parameters that influence the system performance. Experimental tests were then used to identify the values of such parameters. Finally, numerical simulations and experimental tests have been performed to verify the effectiveness of a PWM–PID controller-based co-operative agonist–antagonist control strategy.

References

1. V. Bundhoo, E. Haslam, B. Birch and E. J. Park, "A shape memory alloy based tendon-driven actuation system for biomimetic artificial fingers, part I: Design and evaluation," *Robotica* **27**(1), 131–146 (2009).
2. T. Waram, *Actuator Design Using Shape Memory Alloys* (TC Waram Publishing, Hamilton, ON, Canada, 1993).
3. J. L. McNichols and J. S. Cory, "Thermodynamics of nitinol," *J. Appl. Phys.* **61**(3), 972–984 (1987).
4. C. Liang and C. A. Rogers, "Design of shape memory alloy actuators," *J. Mech. Des.* **114**, 223–230 (1992).
5. M. H. Elahinia and H. Ashrafiuon, "Nonlinear control of a shape memory alloy actuated manipulator," *J. Vib. Acoust.* **124**, 566–575 (2002).
6. C. Liang and C. A. Rogers, "Design of shape memory alloy springs with applications in vibration control," *J. Vib. Acoust.* **115**, 129–135 (1993).
7. A. Y. N. Sofla, D. M. Elzey and H. N. G. Wadley, "Two-way antagonistic shape actuation based on the one-way shape memory effect," *J. Intell. Mater. Syst. Struct.* **19**(9), 1017–1027 (2008).
8. S. Yan, X. Liu, F. Xu and J. Wang, "A gripper actuated by a pair of differential SMA springs," *J. Intell. Syst. Struct.* **18**, 459–466 (2007).
9. S. Kim and M. Cho, "Numerical simulation of a double SMA wire actuator using the two-way shape memory effect of SMA," *Smart Mater. Struct.* **16**, 372–381 (2007).
10. K. Singh, J. Sirohi and I. Chopra, "An improved shape memory alloy actuator for rotor blade tracking," *J. Intell. Mater. Syst. Struct.* **14**, 767–786 (2003).
11. M. J. Mosley and C. Mavroidis, "Experimental nonlinear dynamics of a shape memory alloy wire bundle actuator," *J.. Dyn. Syst. Meas. Control* **123**, 103–112 (2001).
12. G. Song, "Design and control of a nitinol wire actuated rotary servo," *Smart Mater. Struct.* **16**, 1796–1801 (2007).
13. H. Ashrafiuon, M. Mojtaba, and M. H. Elahinia, "Position control of a three-link shape memory alloy actuated robot," *J. Intell. Mater. Syst. Struct.* **17**, 381–392 (2006).
14. A. Paiva and M. A. Savi, "An overview of constitutive models for shape memory alloys," *Math. Probl. Eng.* **2006**, 1–30 (2005).
15. S. De la Flor, C. Urbina and F. Ferrando, "Constitutive model of shape memory alloys: Theoretical formulation and

https://doi.org/10.1017/S0263574709990324 Published online by Cambridge University Press

experimental validation," *Mater. Sci. Eng. A* **427**, 112–122 (2006).
16. K. Tanaka, "A thermomechanical sketch of shape memory effect: One-dimensional tensile behaviour," *Res. Mech.* **18**, 251–263 (1986).
17. I. Mihalcz, "Fundamental characteristics and design method for nickel-titanium shape memory alloy," *Period. Politech. Ser. Mech. Eng.* **45**(1), 75–86 (2001).
18. S. M. Dutta and H. G. Fathi, "Differential hysteresis modeling of a shape memory alloy wire actuator," *IEEE/ASME Trans. Mechatronics* **10**(2), 189–197 (2005).
19. Z. Bo and D. C. Lagoudas, "Thermomechanical modeling of polycrystalline SMAs under cyclic loading, part IV: Modeling of minor hysteresis loops," *Int. J. Eng. Sci.* **37**, 1205–1249 (1999).
20. B. Choi, Y. Lee and B. Choi, "Fast Preisach modeling method for shape memory alloy actuators using major hysteresis loops", *Smart Mater. Struct.* **13**, 1069–1080 (2004).
21. J. H. Lienhard IV and J. H. Lienhard V, *A Heat Transfer Textbook* (Phlogiston Press, Cambridge, MA, 2008).
22. G. Song and N. Ma, "Control of shape memory alloy actuators using pulse-width pulse-frequency (PWPF) modulation," *J. Intell. Mater. Syst. Struct.* **14**, 15–22 (2003).
23. A. D. Price, A. Jnifene and H. E. Naguib, "Design and control of a shape memory alloy based dexterous robot hand," *Smart Mater. Struct.* **16**, 1401–1414 (2007).
24. S. Choi, "Position control of a single-link mechanism activated by shape memory alloy springs: Experimental results," *Smart Mater. Struct.* **15**, 51–58 (2006).
25. K. Arai, S. Aramai and K. Yanagisawa, "Continuous System Modeling of Shape Memory Alloy (SMA) for Control Analysis," *Proceedings of IEEE International Symposium on Micromechatronics and Human Science*, Nagoya, Japan (1994) pp. 97–99.
26. K. Arai, S. Aramai and K. Yanagisawa, "Feedback Linearization of SMA (shape memory alloy)," *Proceedings of the 34th SICE Annual Conference* (1995) pp. 519–522.
27. P. Kumagai, A. Hozian and M. Kirkland, "Neuro-Fuzzy Model Based Feed-Back Controller for Shape Memory Alloy Actuators," *Proceedings of SPIE* 3984 (2000) pp. 291–299.
28. F. P. Beer, J. E Russel and J. T. DeWolf, *Mechanics of Materials* (McGraw-Hill, New York, 2002).

https://doi.org/10.1017/S0263574709990324 Published online by Cambridge University Press